Mechanism insight into oxygen vacancy-dependent effect in Fe_1/TiO_2 single-atom catalyst for highly enhanced photo-Fenton mineralization of phenol

Man Yang [a,1], Haibo Li [a,1], Fenli Liu [b,1], Shaodong Sun [a,*], Jing Mei [a], Yuxiang Jiao [a], Jie Cui [a], Yang Xu [a], Hailiang Song [a], Zongfan Duan [a], Wengang Liu [c,*], Yujing Ren [b,d,**]

[a] Engineering Research Center of Conducting Materials and Composite Technology, Ministry of Education; Shaanxi Engineering Research Center of Metal-Based Heterogeneous Materials and Advanced Manufacturing Technology; Shaanxi Province Key Laboratory for Electrical Materials and Infiltration Technology; School of Materials Science and Engineering, Xi'an University of Technology, Xi'an, Shaanxi 710048, People's Republic of China

[b] Interdisciplinary Research Center of Biology & Catalysis; School of Life Sciences, Northwestern Polytechnical University, Xi'an, Shaanxi 710072, People's Republic of China

[c] College of Materials Science and Engineering , Qingdao University of Science and Technology, Qingdao, Shandong 266042, People's Republic of China

[d] Chongqing Innovation Center, Northwestern Polytechnical University, Chongqing, Chongqing 401135, People's Republic of China

A R T I C L E I N F O

A B S T R A C T

This study develops a highly efficient Fe_1/TiO_2-O_V single-atom catalyst to explore the synergistic effect in the photo-Fenton mineralization of phenol. Via using diverse in-situ spectroscopies and density functional theory calculations, the catalytic mechanism is unraveled. That is, oxygen vacancies can significantly accelerate photogenerated charge separation and oriented delivery to Fe_1 single atoms for fast generation of reactive oxygen species, as well as promote the selective adsorption/activation of phenol. As a result, the C-H bonds on phenol were deeply oxidized (conversion: > 91%), accompanied by the mineralization of the benzene ring, with CO_2 and H_2O as end products (mineralization rate: 66%). Such concerted catalysis between Fe single atoms and oxygen vacancies results in a high reactivity for phenol photo-Fenton mineralization, which is superior to most reported transition-metal-based catalysts. Our finding is expected to provide guidance for designing high-efficiency heterogeneous catalysts in the photo-Fenton catalytic process.

1. Introduction

With the rapid upsurge in industrialization and modernization, noxious contaminants have been released into water bodies, which led to the destruction of the human future [1,2]. Among the various pollutants, the extensive amounts of phenol in wastewater discharged from chemical industries are found to be more lethal, seriously relating to environmental threats and threatening human existence [3–6]. Even in some European countries, where the threshold value of phenol is set at 0.5 ppm, phenol can still have an impact on human health and the environment [7]. Nevertheless, phenol is difficult to remove due to its perseverance and refractoriness of the benzene ring. In recent years, extensive efforts have been made to develop an efficient water purification technique that can be effectively utilized to remove phenol from water resources. Among them, catalytic oxidation is widely regarded as a highly effective destructive method [8–10]. Nevertheless, traditional thermocatalysis and photothermocatalysis have very fatal drawbacks, such as high cost and low stability. Because of its mild conditions, eco-friendliness, high efficiency, and minimal by-products, photo-Fenton catalytic oxidation is a promising method for phenol mineralization with extensive practical application possibilities [11,12]. The primary issues in this field currently are the ring-opening difficulties of phenol and the ambiguous surface reaction mechanism.

Heterogeneous photo-Fenton catalytic oxidation reactions involve three consecutive steps: (i) the adsorption of the reactants, (ii) the charge generation and transfer for reactive oxygen species (ROS)

---

generation, and (iii) the surface reaction and product desorption. Firstly, for step one, surface oxygen vacancies (O_V) have been verified by some studies to effectively facilitate the adsorption of the hydroxyl group [13, 14]. The adsorption of hydroxyl is conducive to the following surface reaction of phenol oxidation. Then, for ROS generation, single-atom metal is regarded as the effective active site in both Fenton-catalytic and photocatalytic ROS generation owing to its metal reactive centers with a high density of electrons [15–20]. For instance, Duan et al. reported that Fe^{2+}/Fe^{3+} redox electricity pairs of Fe single atom exhibited the most effective Fenton catalytic activity among transition metals due to the unique $4d$ electron configuration for ROS generation [21]. Xiong et al. revealed that the single-atom metals were able to work as an electron sink in photocatalysts, which is capable of accelerating the production of superoxide radicals in photocatalysis [16]. According to the above results, the metal single atoms in the photocatalyst can also inject electrons into the Fenton process for ROS production (Fe^{2+}/Fe^{3+} redox). However, the recombination of photogenerated electron-hole pairs arising from random electron transfer significantly decreases the photogenerated electron utilization efficiency. Thus, it still remains a considerable challenge for effective separation and oriented delivery of photogenerated electrons to generate ROS.

Generally, support plays a crucial role in charge separation, single atom deposition, and charge transfer to the metal center [22–24]. Thus, the ROS generation in the photo-Fenton reaction is closely related to the electron density of the Fe single center, and the electron density of the Fe reactive center relies on the properties of support. In this instance, it is very desired to control the separation efficiency and migration behavior of photogenerated electrons by effective support modification. Previous studies suggest that oxygen vacancies on support provide the sites for the deposition of single-atom metal, which also limits the domain between single atom sites and oxygen vacancies [25,26]. Because the oxygen vacancies serve as the electron trap states, oriented delivery and effective separation of photogenerated electrons may be realized, which can further drive the photoexcited electrons directionally transfer from oxygen vacancies to Fe single site in this domain [18,27]. Furthermore, the introduction of both single-atom metal and oxygen vacancies into support can import the impurity level below the conduction band to narrow the band gap, which results in the improvement of photons absorption and charge separation capacity, leading to more photogenerated electrons [28,29]. Inspired by above mentions, it is meaningful to fabricate an O_V-rich single-atom catalyst. However, little attention has been paid to the roles of single atoms combining oxygen vacancies in the photo-Fenton catalytic oxidation of phenol.

Herein, we proposed an oxygen vacancies engineering strategy in Fe_1/TiO_2 single-atom catalyst, which can promote the photogenerated electrons on the Fe single site for ROS formation, as well as serve as an adsorption site for phenol. The Fe_1/TiO_2-O_V catalyst was developed by the hydrothermal method and molten-salt method. Firstly, the TiO_2 was treated at different temperature or time to fabricate TiO_2-O_V with different concentrations of oxygen vacancies. Then, earth-abundant Fe single atoms were precisely anchored on TiO_2 by a novel molten-salt method. The as-obtained Fe_1/TiO_2-O_V catalysts were employed in the photo-Fenton for phenol removal, which exhibited remarkable phenol oxidation reactivity. The morphological, physicochemical, and photoelectric properties of Fe_1/TiO_2-O_V catalyst revealed that the introduction of Fe single atoms significantly enhanced the charge separation and transfer, especially in the presence of oxygen vacancies, which demonstrated the synergy between Fe single atoms and oxygen vacancies. Furthermore, the adsorbed and catalytic behavior for phenol oxidation were investigated by in-situ Raman, ATR-IR spectra and DFT calculations to reveal the key factors to photo-Fenton activity and clarify the photo-Fenton catalytic mineralization mechanism for phenol. We proposed that the hydroxyl group of phenol was adsorbed on the unsaturated coordination of TiO_2, and then activated by the ROS to ring-opening intermediates, finally to CO_2 and H_2O. The main ROS of $\bullet O_2^-$, $^1O_2$, $\bullet OH$ and $\bullet SO_4^-$ were generated on the Fe single atoms by the

enrichment of photogenerated electrons. GC-MS was used to uncover the detailed mineralization pathways toward phenol over the Fe_1/TiO_2-O_V catalyst.

2. Experimental section

2.1. Catalyst synthesis

TiO_2 support with different oxygen vacancy content was prepared by the hydrothermal method: 1 g of TiO_2 was dispersed into 40 mL ethylene glycol with stirring for 30 min, and then the suspension was transferred to a Teflon-lined stainless steel autoclave with a volume of 100 mL and heated at needed temperature (160 °C, 180 °C, 200 °C, 220 °C) for a certain time (6 h, 12 h, 24 h). After naturally cooling to room temperature, the solid product was centrifuged, and washed three times with deionized water and alcohol, respectively. The TiO_2 support with different oxygen vacancy content (TiO_2-O_V) was obtained after drying in an oven at 60 °C.

Fe_1/TiO_2-O_V and Fe_1/TiO_2 catalysts were prepared by the molten-salt method: 1 g of TiO_2-O_V or TiO_2, 0.9 g of LiCl, 1.1 g of KCl and a certain amount (15 mg, 20 mg, 30 mg, 40 mg, 60 mg) of $FeCl_2 \bullet 4 H_2O$ were mixed and ground for 30 min, followed with calcination in the tubular furnace at 500 °C for 2 h under N_2 atmosphere. After cooling to room temperature, the products were washed three times with deionized water and alcohol, respectively. The Fe_1/TiO_2-O_V was obtained after drying in an oven at 60 °C.

2.2. Structure, morphology and composition characterizations

X-ray diffraction (XRD) patterns were obtained on an XRD-7000 X-ray diffractometer equipped with a Cu target. Scanning electron microscopy (SEM) images were observed on a JEM-7000 F scanning electron microscope. The working voltage of the scanning electron microscope was 15 kV, equipped with an energy dispersive spectroscopy (EDS) microanalysis system. Atomic high-angle annular dark-field scanning transmission electron microscopy (AC-HAADF-STEM) and energy dispersive spectroscopy were recorded on a FEI Themis Z microscope equipped with spherical aberration corrector and operated at 300 kV, with a guaranteed resolution of 0.06 nm. Nitrogen adsorption-desorption measurements were performed at 77 K on a Micromeritics ASAP 2460 instrument. The Raman spectrum was obtained in the Raman spectrometer of DXR2 Xi. Electron paramagnetic resonance (EPR) spectra were obtained at Bruker EMX nano benchtop electron paramagnetic resonance spectrometer. X-ray photoelectron spectroscopy (XPS) images were obtained by XPS of ESCALAB250. The concentration of iron in the catalyst and solution was determined by inductively coupled plasma optical emission spectrometry (ICP-OES), IRIS Intrepid II, USA (Table S1). The X-ray absorption fine structure spectrum (XAFS) diagram was obtained by using the BL14W1 beam test of synchrotron radiation light source (SSRF). The attenuated total reflection infrared (ATR-IR) spectroscopy was acquired with a BRUKER Equinox 55 spectrometer equipped with a DLaTGS detector. The residual total organic carbon (TOC) in the solution was measured by a TOC analyzer (Elementar, Germany). Thermogravimetry and differential thermal analysis (TGA) were performed on a STA 449 F3 device from 30 °C to 600 °C with a ramping rate of 10 °C/min in a stream of Ar. The intermediate products were detected by gas chromatography–mass spectrometer (GC-MS, ISQ, Thermo) with pure He as the mobile phase.

2.3. Photochemical properties

UV–vis diffuse reflectance spectra (DRS) were recorded by U-4100UV–VIS–NIR Hitachi using $BaSO_4$ as the reflectance standard material and the measurement range was 200–800 nm. Photoluminescence (PL) was characterized by FLS1000 with at room temperature and the excitation wavelength was 365 nm. The photocurrent and
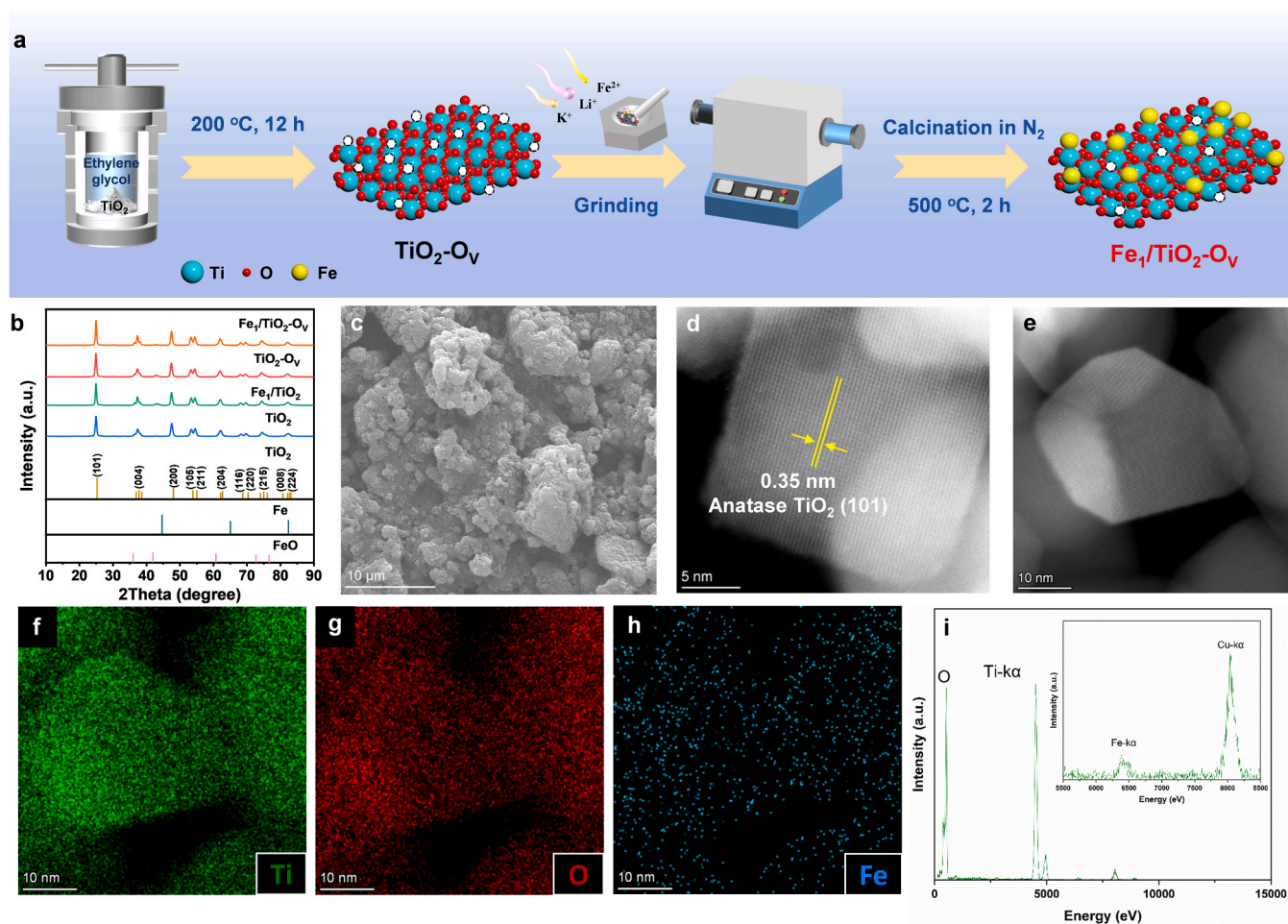
Fig. 1. (a) The schematic for the synthesis process of Fe_1/TiO_2-O_V catalyst; (b) XRD patterns, (c) SEM image, (d,e) AC-HAADF-STEM images and (f-i) corresponding EDS mapping results of Fe_1/TiO_2-O_V catalyst.

electrochemical impedance spectroscopy (EIS) were evaluated on the Shanghai Chenhua electrochemical system (CHI660E) with a three-electrode system. Na_2SO_4 solution (100 mL, 0.2 M, pH = 7), Ag/AgCl electrode, and platinum net were used as electrolyte solution, reference electrode, and counter electrode respectively. Indium tin oxide (ITO) glasses covered with catalyst were working electrodes and the preparation process was as follows: First, 10 mg catalyst was dissolved in 1 mL water to form the homogeneous solution by sonication for 20 min. Subsequently, 20 μL Nafion was dispersed to the above solution. Then, 100 μL of the suspension was added to the surface of ITO glass (1 cm×1 cm). Eventually, the working electrode was obtained. During the tests, an Xe lamp (300 W) with a cut-off filter (λ > 420 nm) was used as the light source.

2.4. Photo-Fenton catalytic performance

The structure of photocatalytic reactor (Fig. S1) and detailed information of catalyst optical parameters, including extinction coefficient, reactor optical thickness and total rate of photon absorption, is illustrated in Supporting Information. The detailed process of photocatalytic degradation of phenol solution is as follows. 10 mg of catalyst was dispersed into a 100 mL beaker containing 50 mL phenol aqueous solution (10 mg/L). Then, it was stirred at 500 rpm to reach the adsorption-desorption equilibrium between the solution and sample in the absence of light. After 60 min, 10 mg of potassium peroxymonosulfate (PMS, $KHSO_5$) was added into the reaction system, in the meantime, the beaker was irradiated with visible light (λ > 420 nm) of

300 W Xe lamp at room temperature. With continuous stirring, the absorbance of 4 mL solution at 269 nm was measured by UV–vis spectrophotometer at an interval of 30 min. The calculation formula for photocatalytic efficiency is as follows:

$$\text{Photocatalytic effciency} = \frac{C_0 - C_t}{C_0} \times 100\%$$

C_0: the initial absorbance, C_t: the absorbance at specific time.

2.5. Computational methodology

The adsorption energy (E_a) of phenol adsorbate on Fe@TiO_2(101) surface and Fe@TiO_2(101)-O_V surface was calculated based on plane-wave pseudopotential density functional theory using CASTEP code. The change-correlation interaction was treated by the generalized gradient approximation (GGA) with PBE functional. The plane wave cutoff energy based on the ultrasoft pseudopotential is set as 450 eV with LBFGS method for all the geometry optimizations. The k-point mesh with a spacing of 0.04 Å^{-1} generated by the Monkhorst-Pack scheme for Brillouin zone sampling. To obtain the convergent results in the geometry optimization step, the tolerance of energy, maximum force, maximum ionic displacement, and self-consistent field (SCF) is 2.0×10^{-5} eV/atom, 0.05 eV/Å, 0.002Å and 2.0×10^{-6} eV/atom, respectively. In this work, the TiO_2 (101) surface slab was constructed with a 2×3 unit cell composed of three atomic layers. The bottom layer was constrained at their lattice positions. The vacuum space along the z direction was set to be 15 Å to avoid interactions between periodic slabs.
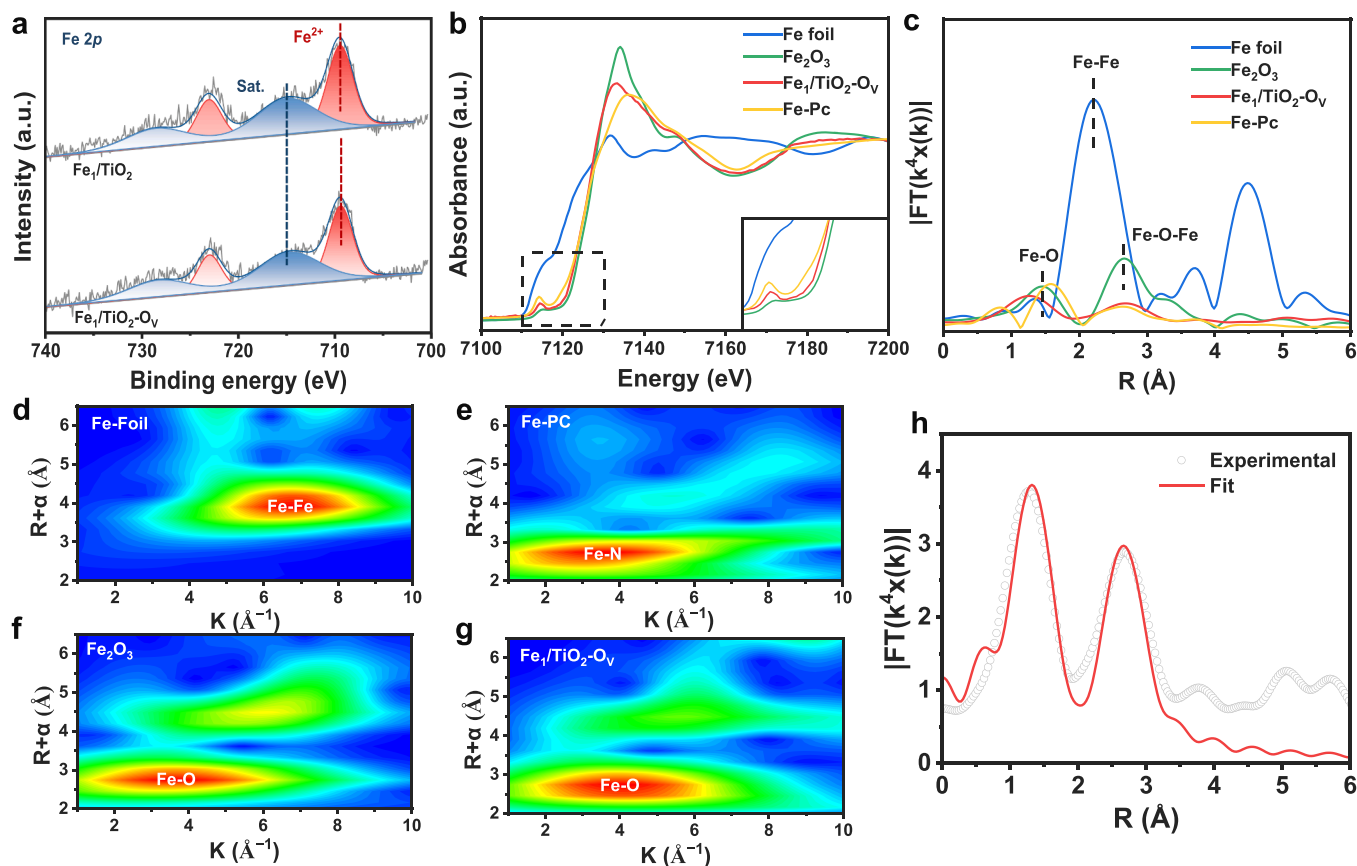
Fig. 2. (a) Fe 2p XPS spectra of Fe$_1$/TiO$_2$-O$_V$ and Fe$_1$/TiO$_2$; (b) Fe K-edge normalized XANES spectra of Fe$_1$/TiO$_2$-O$_V$ and references; (c) Fe K-edge EXAFS spectra in R space for Fe$_1$/TiO$_2$-O$_V$ and references; (d-g) Wavelet transform analysis for the k^2-weighted EXAFS signals of Fe foil (d), Fe-Pc (e), Fe$_2$O$_3$ (f) and Fe$_1$/TiO$_2$-O$_V$ catalyst (g); (h) Fe K-edge R space EXAFS fitting results of the Fe$_1$/TiO$_2$-O$_V$.

The adsorption energy (E$_a$) of adsorbate (phenol) was defined as:

$$E_a = E_{adsorbate-surface} - E_{adsorbate} - E_{surface}$$

where E$_{adsorbate-surface}$, E$_{surface}$ and E$_{adsorbate}$ represent the energy of adsorbate adsorbed on the surface slab, the energy of surface and the energy of adsorbate, respectively.

3. Results and discussion

3.1. Preparation and identification of Fe single-atom site

To better stabilize single-atoms and engineer the domain of single-atoms and defects, a successive hydrothermal and molten-salt method was developed in present work. TiO$_2$-O$_V$ containing different oxygen vacancies was synthesized by hydrothermal method using ethylene glycol as a reductant. FeCl$_2$•4 H$_2$O was used as a Fe source to prepare single-atom catalyst (Fe$_1$/TiO$_2$-O$_V$) by molten-salt method, as shown in Fig. 1a. Firstly, the crystal structure and chemical composition of the TiO$_2$, TiO$_2$-O$_V$, Fe$_1$/TiO$_2$ and as-prepared Fe$_1$/TiO$_2$-O$_V$ were determined by X-ray diffraction (XRD). In Fig. 1b, the obvious peaks of the four samples are indexed to anatase TiO$_2$, according to JCPDS No. 21–1272, suggesting the crystalline structure of TiO$_2$ was maintained without destruction during hydrothermal process or hyperthermal molten-salt. No obvious peak attributed to Fe species was detected, which may be attributed to the high dispersion or low content of Fe.

On this basis, the scanning electron microscope (SEM) and aberration-corrected high-angle annular dark-field scanning transmission electron microscopy (AC-HAADF-STEM) analysis were used to examine the morphologies and microstructures of these four catalysts. Obviously, the SEM images showed that all catalysts display a stacked structure composed of uneven size and randomly stack nanosheets (Fig. 1c and S2), further confirming the structural stability of TiO$_2$. Moreover, the AC-HAADF-STEM images clearly showed the stack of layers (Fig. 1d and e), agreeing with the SEM. Furthermore, as shown in Figs. d, e and S3 of AC-HAADF-STEM images, it was hard to observe Fe species, indicating scarcely any large iron or iron oxide particles in the Fe$_1$/TiO$_2$-O$_V$ catalyst. Though no bright spots could be distinguished from the AC-HAADF-STEM images due to the of atomic number between Fe (Z = 26) and Ti (Z = 22) [16,30], EDS scanning showed uniform distribution of iron species, with more than triple signals compared to the errors in the scanned areas (Figs. S4–6, Table S2), which confirmed the existence of highly dispersed Fe species (also supported by evidence of Fe-K characteristic peak in overall EDS spectra, Figs. S4–6). On this basis, an independent TiO$_2$ particle with the size of ~30 nm had been analyzed (Fig. 1e-i, Table S3). In about 40 nm × 40 nm ROI for corresponding EDS mapping, we used a 1024 × 1024 mapping resolution giving a sampling pixel size as small as ~0.04 nm to probe the localized elemental distribution. In this case for a ~1 nm nanoparticle of Fe species supported on the TiO$_2$ surface, there would be 625 probing pixels (25 × 25) of EDS analysis to firmly depict the particle/cluster's presence, which could be guaranteed by the high detection efficiency of the Super X EDS equipped on the microscope. Since there was no aggregation but homogeneous dispersion of Fe as detected by EDS mapping, it was reasonably deduced the atomic dispersion of Fe on the TiO$_2$ surface.

For a clearer understanding of the microstructure and physicochemical properties of Fe$_1$/TiO$_2$-O$_V$, the chemical states of Fe species were characterized by X-ray photoelectron spectroscopy (XPS) (Fig. 2a and Table S4). The characteristic Fe 2$p_{3/2}$ satellite peak located at approximately 709 eV was present. The peak at 709.3 eV and 709.4 eV, which corresponds to Fe^{2+} [31,32], dominated Fe 2$p_{3/2}$ in Fe$_1$/TiO$_2$-O$_V$
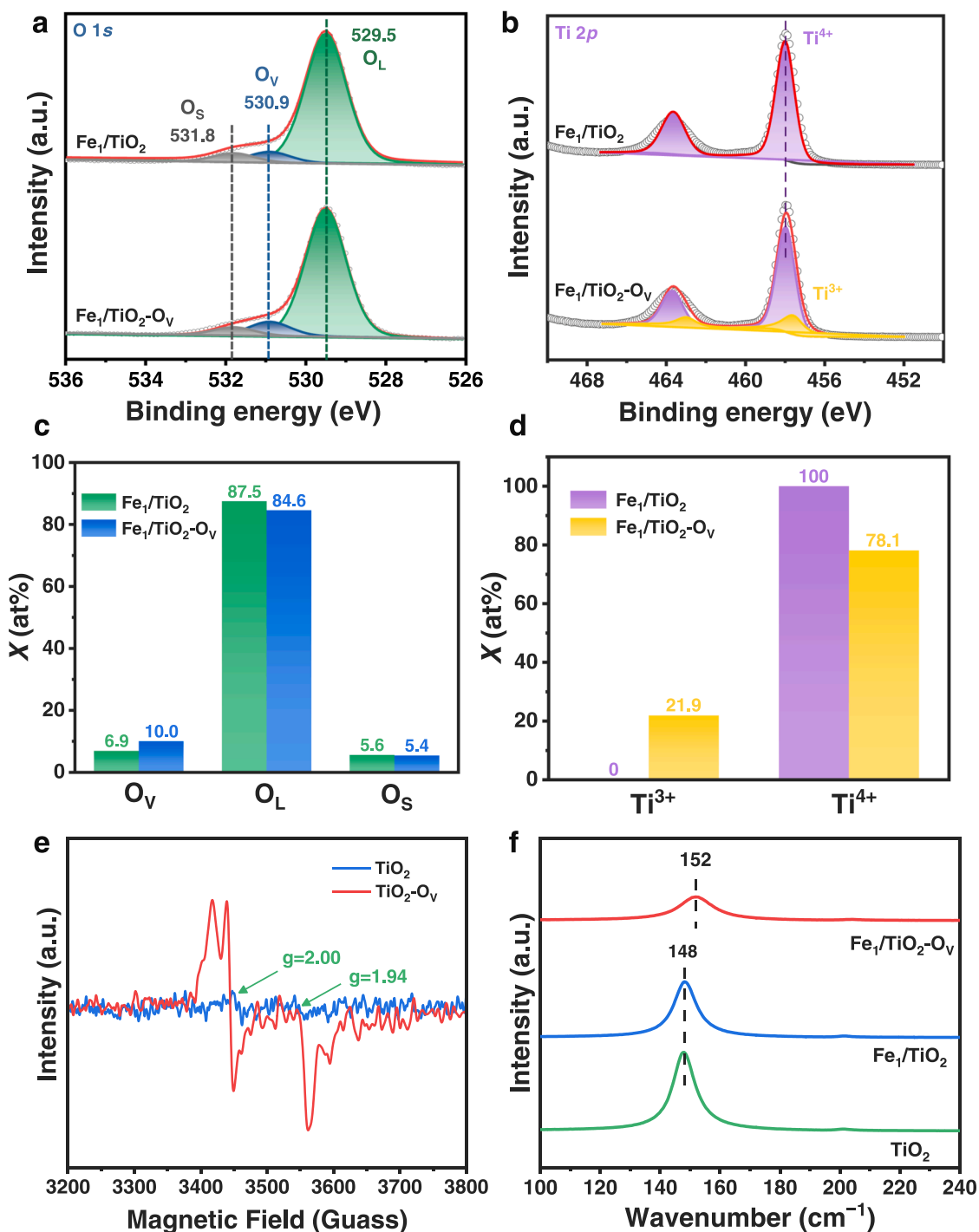
Fig. 3. (a) O 1 s and (b) Ti 2p XPS spectra of Fe$_1$/TiO$_2$-O$_V$ and Fe$_1$/TiO$_2$; (c, d) Molar content (X) of O species in O element and Ti species in Ti element, calculating according to the XPS area. (e) Room-temperature EPR spectra of TiO$_2$-O$_V$ and TiO$_2$ samples; (f) Raman spectra of Fe$_1$/TiO$_2$-O$_V$, Fe$_1$/TiO$_2$ and TiO$_2$ samples.

and Fe$_1$/TiO$_2$, respectively, indicating the molten salt method formed Fe^{2+} single atoms over both TiO$_2$ and TiO$_2$-O$_V$. In the meantime, with the introduction of O$_V$ in Fe$_1$/TiO$_2$, Fe 2p spectra slightly shifted to lower binding energy compared with Fe$_1$/TiO$_2$, demonstrating that oxygen vacancies favored the formation of reaction centers Fe with greater local electron density [18]. Thus, the oxygen vacancies can redistribute the extra electrons to surrounding single Fe sites via the delocalized electronic states of pristine TiO$_2$ [33], resulting in higher local electron density. X-ray absorption near-edge structure (XANES) spectroscopies were used to further establish the chemical state of the iron species over Fe$_1$/TiO$_2$-O$_V$ (Fig. 2b). According to the E$_0$ for Fe$_1$/TiO$_2$-O$_V$, which is

lower than that of Fe$_2$O$_3$ and similar to that of Fe-Pc, it demonstrated Fe atoms had positive charges of +2, agreement with the results of XPS. Furthermore, the coordination environment of Fe single atoms was identified by X-ray absorption fine structure spectra (EXAFS). As can be seen in the Fourier-transformed k^2 weighted EXAFS spectra at the Fe K-edge (Fig. 2c), the Fe$_1$/TiO$_2$-O$_V$ catalyst didn't exhibit any observable peaks at the positions of the Fe-Fe shell, excluding the presence of metallic Fe nanoparticles [34,35]. Likewise, wavelet transform analysis further verified the absence of Fe-Fe scattering, in which only the peaks ascribed to Fe-O bonds were observed in Fe$_1$/TiO$_2$-O$_V$ (Fig. 2d-g). As for the second shell, due to the atomic dispersion of Fe species on TiO$_2$

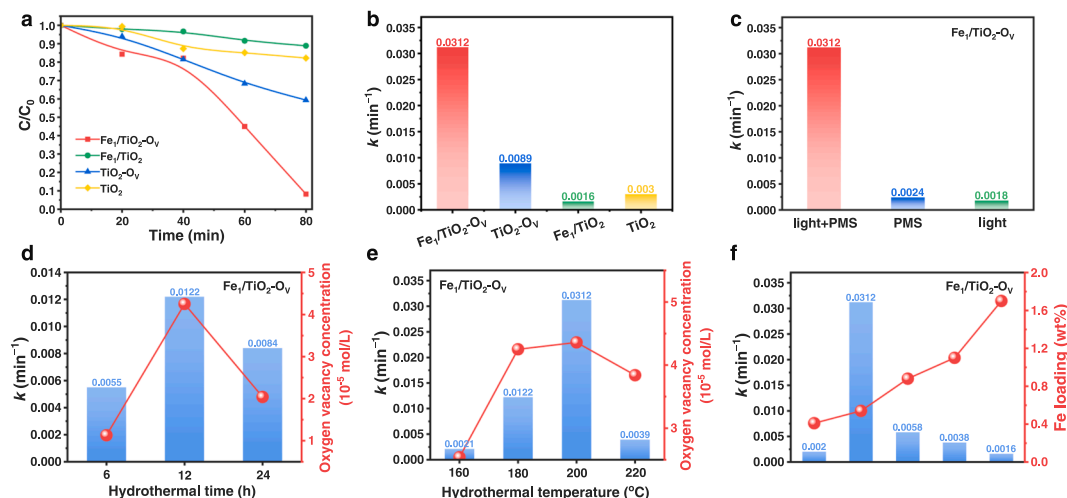**Fig. 4.** (a) Degradation efficiency curve and (b) catalytic kinetics of Fe_1/TiO_2-O_V, TiO_2-O_V, Fe_1/TiO_2 and TiO_2 catalyst systems in the photo-Fenton oxidation for phenol; (c) Catalytic kinetics of Fe_1/TiO_2-O_V catalyst systems in the photocatalysis, Fenton catalysis and photo-Fenton catalysis for phenol; The effects of oxygen vacancy concentration that modulated by (d) hydrothermal time and (e) hydrothermal temperature in Fe_1/TiO_2-O_V on the photo-Fenton catalytic activity for phenol; (f) The effects of Fe single atom loading in Fe_1/TiO_2-O_V on the photo-Fenton catalytic activity for phenol.

surface, the small but detectable peak at 2.7 Å distance could be reasonably ascribed to Fe-Ti coordination with oxygen atom as the bridge (Fe-O-Ti) [36]. The best-fitting results of EXAFS exhibited the Fe-O coordination number was 4.8 (Fig. 2h and Table S5), which implied each isolated iron atom coordinated with five oxygen atoms to form a Fe_1O_5 structure. Hence, it could be confirmed the atomically dispersed Fe species on TiO_2 with a positive charge of +2.

3.2. Identification of oxygen vacancies

To examine the surface property of several catalysts, high-resolution O 1 *s* XPS spectra were conducted. As shown in Fig. 3a, the lattice oxygen (O_L) over the TiO_2 peak was positioned at ca. 529.5 eV, the oxygen vacancy peak was at ca. 530.9 eV and the surface hydroxyl groups (O_S) was at ca. 531.8 eV. Together, these three peaks made up the O 1 *s* core level of both Fe_1/TiO_2 and Fe_1/TiO_2-O_V catalysts [28,29,37]. Significantly, the percentage of O_V in the Fe_1/TiO_2-O_V catalyst was 10.0%, which was higher than that in Fe_1/TiO_2 (6.9%) (Fig. 3c and Table S4), strongly demonstrating the successful introduction of O_V in pristine TiO_2. Likewise, the Ti 2*p* XPS spectra was also analyzed (Fig. 3b) [38], and the content of Ti^{3+} ($(Ti^{3+} / (Ti^{3+} + Ti^{4+}))$) was calculated in Fig. 3d and Table S4. It revealed that Fe_1/TiO_2-O_V had a higher concentration of unsaturated coordination. Therefore, the XPS results could confirm that the surface O_V was successfully induced.

Furthermore, the introduction of bulk O_V was determined by electron paramagnetic resonance (EPR) and Raman spectra. To avoid the effect of single electrons in Fe single atoms on the determination for O_V, TiO_2, and TiO_2-O_V were employed to record the EPR spectra. As shown in Fig. 3e, the peak with g = 2.00 is attributed to oxygen vacancy, and the peak with g = 1.94 is assigned to Ti^{3+} [39,40]. The obvious enhancement of both peaks in TiO_2-O_V compared to TiO_2 suggested that the concentration of bulk oxygen vacancies in TiO_2-O_V was significantly enhanced by the hydrothermal process compared to pristine TiO_2. Moreover, the concentration of O_V could be well regulated by hydrothermal temperature and time (Fig. S7a-b). It showed that the largest concentration of O_V was obtained at the hydrothermal conditions of 200 °C for 12 h. In good agreement with EPR spectra, the ν(O-Ti-O) modes in Raman spectra of Fe_1/TiO_2-O_V catalyst slightly blueshifted to 152 cm^{-1} compared to Fe_1/TiO_2 catalyst (148 cm^{-1}) (Fig. 3f), demonstrating the enhancement of O_V in Fe_1/TiO_2-O_V catalyst [41]. Notably, the almost identical Raman spectra of TiO_2 support and Fe_1/TiO_2 suggested no O_V was generated with Fe single atoms loading. Combining the

results of XPS, it could be concluded that the surface oxygen vacancies and bulk oxygen vacancies were successfully constructed in the Fe_1/TiO_2-O_V catalyst.

In order to investigate the effect of O_V generation on the specific surface area of samples, the nitrogen adsorption-desorption isotherms of the Fe_1/TiO_2-O_V and Fe_1/TiO_2 were recorded. As shown in Fig. S8a, it showed type IV with an H_1 hysteresis loop, which indicated that the presence of mesoporous structures [42], consistent with the pore size distribution curves (Fig. S8b). The results were further summarized in Table S6, it can be seen Fe_1/TiO_2-O_V and Fe_1/TiO_2 samples possessed similar specific surface area and pore size, indicating that the difference in Fe_1/TiO_2-O_V and Fe_1/TiO_2 catalytic activity was not directly related to the specific area and pore size.

3.3. Photo-Fenton catalytic performance for phenol degradation

The photo-Fenton oxidation activities toward phenol of the Fe_1/TiO_2-O_V, TiO_2-O_V, Fe_1/TiO_2 and TiO_2 samples were evaluated under the optimum optical thickness of 2.86 (Fig. S9). The removal of phenol as a function of time was displayed in Figs. 4a and 4b. It can be seen that the Fe_1/TiO_2-O_V catalyst exhibited outstanding photo-Fenton activity and rate constant (k_{obs}) that fitted by the first-order reaction for phenol degradation compared to Fe_1/TiO_2, TiO_2-O_V and TiO_2 samples, suggesting the synergy effect between Fe single atoms and oxygen vacancies. Moreover, the synergy effect of light catalysis and Fenton catalysis was also proved by the control experiment in Fig. 4c. Compared to the presence of only visible light or only PMS, the degradation activity enhanced significantly under the combination of light and PMS. In addition, the phenol can't be removed at all without catalyst in photo-Fenton conditions (Fig. S10). Due to the vital role of oxygen vacancies and Fe single atoms, we further explored the optimal O_V concentration and Fe loading for photo-Fenton catalytic performance toward phenol. The photo-Fenton catalytic oxidation activity towards phenol as a function of oxygen vacancy concentration in Fe_1/TiO_2-O_V catalyst that was calculated based on EPR results was shown in Fig. 4d and e. As expected, the photo-Fenton catalytic oxidation activity towards phenol was positively correlated with oxygen vacancy concentration. The Fe_1/TiO_2-O_V catalyst with the highest O_V concentration obtained at 200 °C and 12 h hydrothermal condition exhibited superior photo-Fenton catalytic oxidation activity towards phenol. Moreover, the optimal Fe loading was determined to be 0.54% (Fig. 4f). Under the optimal reaction conditions of 10 mg catalyst dosage (Fig. S11), 10 mg/L phenol
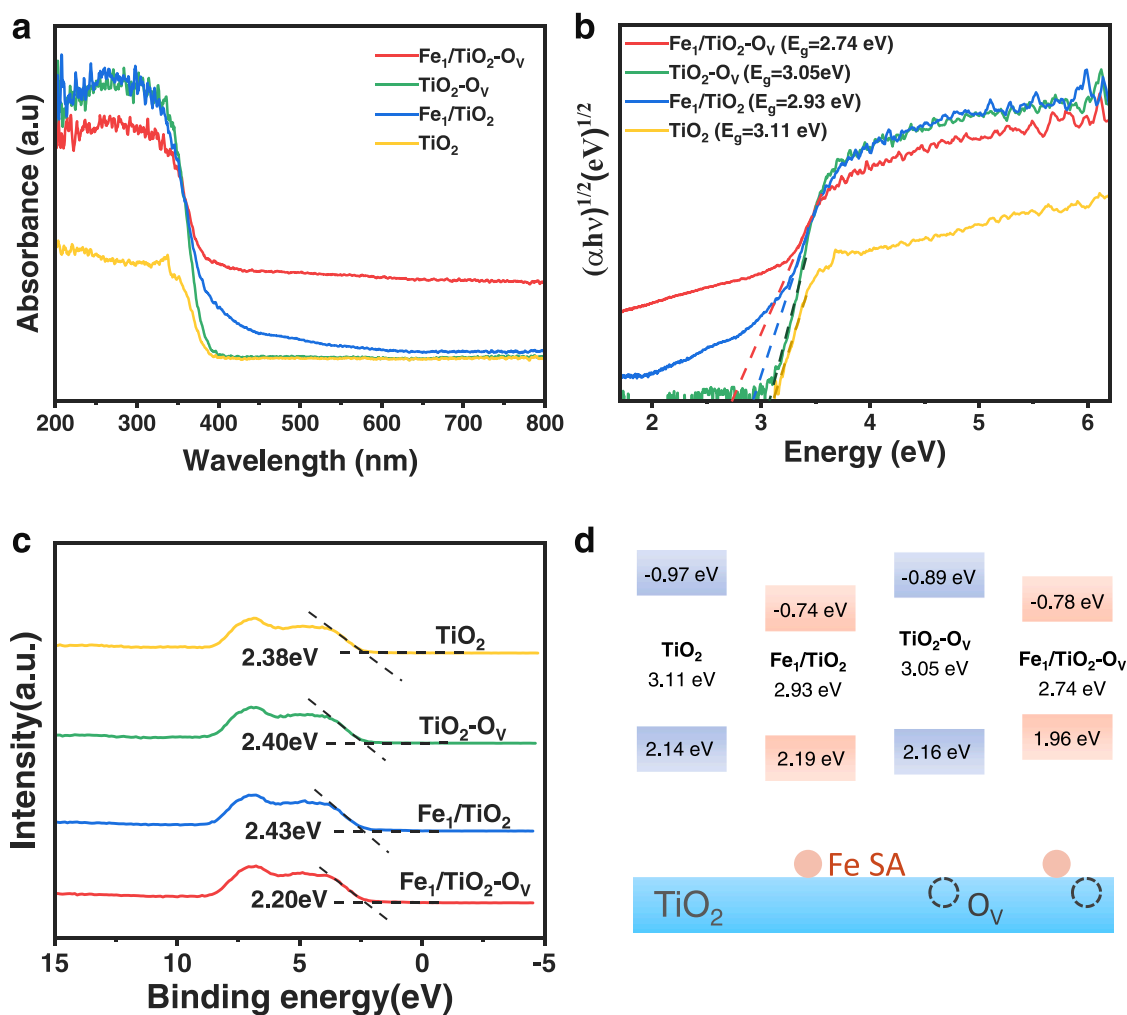
Fig. 5. (a) UV-Vis diffuse reflectance spectra, (b) band gap (E_g), (c) VB XPS spectra and (d) band edge alignments of Fe_1/TiO_2-O_V, Fe_1/TiO_2, TiO_2-O_V and TiO_2 samples.

concentration (Fig. S12) and 10 mg PMS dosage (Fig. S13), the Fe_1/TiO_2-O_V catalyst can achieve the removal for phenol as high as 91.8% at 80 min, and the k_{obs} for phenol removal kinetics over Fe_1/TiO_2-O_V catalyst was 0.0312 min^{-1}, which was almost 20 times higher than Fe_1/TiO_2 catalyst without oxygen vacancies. Further decreasing the concentration of phenol to 3 mg/L, the removal kinetics over Fe_1/TiO_2-O_V catalyst can reach 0.0814 min^{-1}. It was more excellent than that of other related photocatalysts in literature, summarized in Table S7 [43–57]. More importantly, the phenol mineralization rate of the Fe_1/TiO_2-O_V catalyst reached 66% that detected by TOC.

Furthermore, we also determined the stability of the Fe_1/TiO_2-O_V catalyst. As shown in Fig. S14, the photo-Fenton catalytic activity of Fe_1/TiO_2-O_V almost maintained after four cycles. Also, no obvious activity loss after 5 h was observed in continuous flow experiment (Fig. S15). In the meanwhile, the ICP-OES, XRD pattern, TEM image and XPS spectra of the Fe_1/TiO_2-O_V-spent catalyst turned out that no distinct change of microstructures or physicochemical properties was obtained (Tables S8 and S9 and Fig. S16), confirming the high stability was maintained in Fe_1/TiO_2-O_V catalyst.

3.4. The generation of ROS

Apparently, the ability of catalysts to produce ROS is a decisive step for photo-Fenton catalytic activity. Therein, light utilization, band structure and charge separation and transfer play a key role in ROS generation. Thus, to elucidate the origin of remarkably enhanced photo-

Fenton catalytic activity of Fe_1/TiO_2-O_V, the influence of oxygen vacancies on light absorption, band structure, charge separation and transfer was carefully investigated. Firstly, the ultraviolet–visible (UV–vis) spectra and valence band (VB) XPS were introduced to examine light response, band gaps and VB position of TiO_2, TiO_2-O_V, Fe_1/TiO_2 and Fe_1/TiO_2-O_V samples. According to the results in Fig. 5a and b, the TiO_2 presented the characteristic absorption band with an onset edge at approximately 366 nm, indicating a bandgap (E_g) of 3.11 eV, consistent with the widely reported value [16,58]. The introduction of oxygen vacancies by the hydrothermal method had a slight effect on the onset edge of TiO_2 ($E_g = 3.05$), however, leading to a significant absorption in the UV-light region. When Fe single atoms were loaded on TiO_2, a slightly enhanced absorption in the visible-light region was observed with the slight narrow of E_g ($E_g = 2.93$). However, the simultaneous introduction of oxygen vacancies and Fe single atoms significantly enhanced the absorption in the visible-light region with the obvious decrease of E_g ($E_g = 2.74$), further confirming the synergy between oxygen vacancies and Fe single atoms. Combining with the XPS-VB spectra (Fig. 5c), in which TiO_2, TiO_2-O_V, Fe_1/TiO_2 and Fe_1/TiO_2-O_V samples showed valence band of 2.38, 2.40, 2.43, 2.20 eV respectively, we obtained the specific band structure of the TiO_2, TiO_2-O_V, Fe_1/TiO_2 and Fe_1/TiO_2-O_V catalysts based on the equation of $E_{VBM-NHE} = \psi + E_{VBM-XPS} - 4.44$ eV ($\psi = 4.20$ eV) and $E_{CBM} = E_{VBM} - E_g$ [59], and showed in Fig. 5d. It can be seen that the conduction band (CB) of Fe_1/TiO_2-O_V (-0.78 eV), Fe_1/TiO_2 (-0.74 eV), TiO_2-O_V (-0.89 eV) and TiO_2 (-0.97 eV) were more negative than $O_2/\bullet O_2^-$ (-0.33 eV),

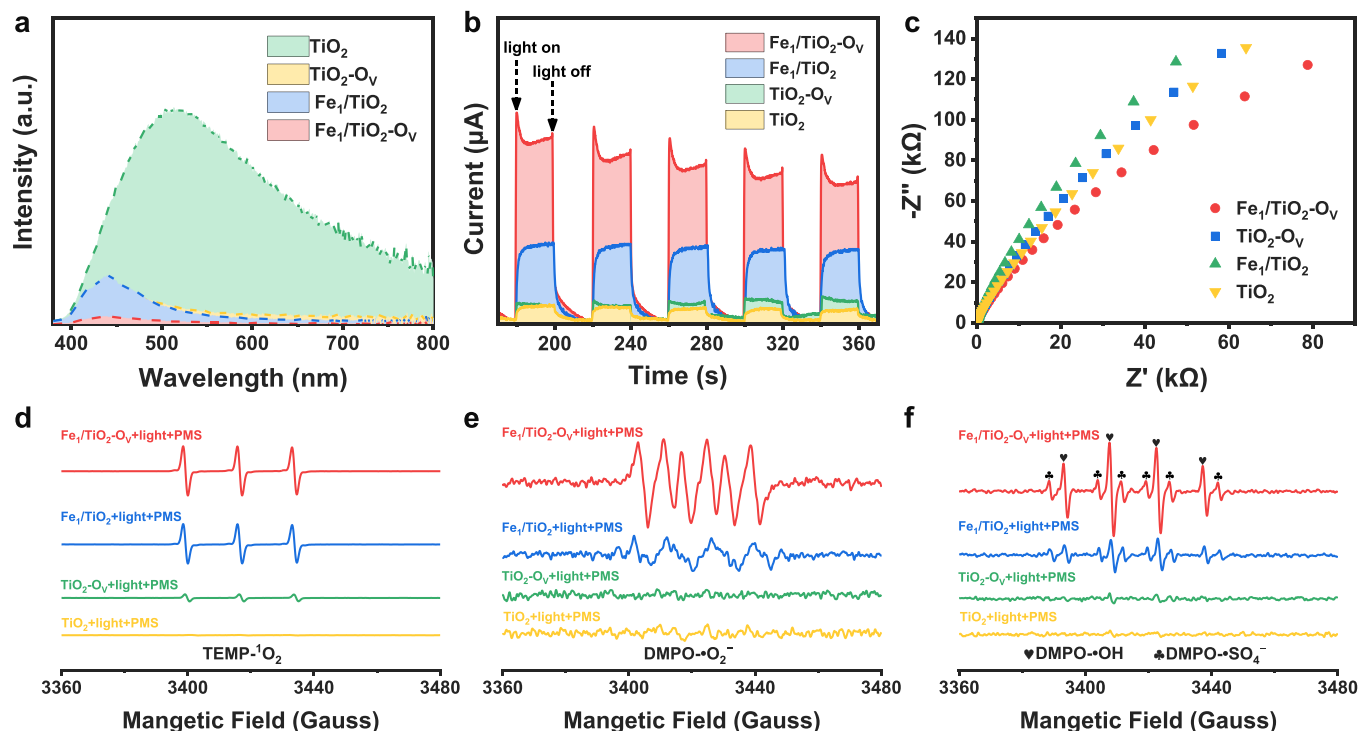**Fig. 6.** (a) Photoluminescence (PL) spectra, (b) photocurrent response curves and (c) electrochemical impedance spectrum (EIS) of Fe_1/TiO_2-O_V, Fe_1/TiO_2, TiO_2-O_V and TiO_2 samples; EPR spectra of (d) $^1O_2$, (e) $\bullet O_2^-$ and (f) $\bullet OH/\bullet SO_4^-$ reactive oxygen species in Fe_1/TiO_2-O_V, Fe_1/TiO_2, TiO_2-O_V and TiO_2 photo-Fenton catalytic systems.

suggesting that these catalysts possessed a stronger ability to produce ROS of $\bullet O_2^-$ ($O_2 + e^- \rightarrow \bullet O_2^-$) in photocatalysis [29]. However, the VB of Fe_1/TiO_2-O_V (1.96 eV), Fe_1/TiO_2 (2.19 eV), TiO_2-O_V (2.16 eV) and TiO_2 (2.14 eV) were still negative than $H_2O/\bullet OH$ (2.40 eV) [60], which indicated it was hard for $\bullet OH$ generation from H_2O via photocatalysis ($H_2O + h^+ \rightarrow \bullet OH + H^+$). Significantly, the narrowest E_g for Fe_1/TiO_2-O_V catalyst suggested the best capacity of charge separation and transfer in Fe_1/TiO_2-O_V, which are vital for ROS generation in photo-Fenton catalysis [61].

Based on this band structure, we further determined the photoelectric properties to investigate the spatial charge separation and transfer over these samples. The intrinsic band-edge photoluminescence (PL) was firstly used to investigate the recombination rate of photogenerated electron-hole pairs [62]. As shown in Fig. 6a, the Fe_1/TiO_2-O_V sample exhibited the lowest PL intensity among the four samples, suggesting the weakest recombination of photogenerated electrons and holes. Consistent with PL results, the highest photocurrent density for Fe_1/TiO_2-O_V sample was obtained under visible-light irradiation (Fig. 6b), confirming the highest efficiency of photogenerated charge separation of the Fe_1/TiO_2-O_V sample. Moreover, the electrochemical impedance spectrum (EIS) was employed to investigate the charge transfer resistance (Rct). The charge transfer resistance is considered to be the composite impedance of the electrode corresponding to the diameter of the semicircle at high frequency [63]. In Fig. 6c, the smallest EIS semicircular diameter of Fe_1/TiO_2-O_V sample under visible-light irradiation indicated the least charge transfer resistance in the Fe_1/TiO_2-O_V sample. Therefore, it can be confirmed that the simultaneous introduction of oxygen vacancies and Fe single atoms synergistically accelerated the photogenerated charge separation and transfer in TiO_2. Combining the XPS spectra of Fe 2*p*, it will effectively enhance the electron density of single Fe sites under light illumination due to the redistributing photogenerated electrons in the oxygen vacancy trap to Fe single site. Whereas, the ROS generation in the photo-Fenton catalytic process was dependent on the photo-separated electrons on the Fe single site, thereby achieving excellent photo-Fenton catalytic performance.

Furthermore, the EPR capturing technique was employed to directly identify the in-situ formed ROS in the presence of PMS under visible-light irradiation (Fig. 6d-f). Apparently, Fe_1/TiO_2-O_V catalyst was able to generate $\bullet OH$, $\bullet SO_4^-$, $\bullet O_2^-$ and $^1O_2$ radicals, whose radical-signal intensities were much higher than those of TiO_2, TiO_2-O_V and Fe_1/TiO_2. It visually confirmed that Fe_1/TiO_2-O_V could produce more ROS to participate in the photo-Fenton catalytic oxidation process of phenol, thus resulting in excellent phenol mineralization ability.

An insight into ROS origination was investigated. Firstly, the degradation activities toward phenol of the Fe_1/TiO_2-O_V in absent of PMS or O_2 was evaluated. As shown in Fig. S17, the removal effectivity of phenol decreased significantly in absent of PMS or O_2, which preliminarily demonstrated the ROS was derived from both PMS and O_2. Furthermore, we employed EPR capturing technique to identify the ROS in absent of PMS and O_2. In Fig. S18, it can be seen the intensity of $\bullet O_2^-$, $^1O_2$, $\bullet OH$, $\bullet SO_4^-$ was decreased obviously in absence of PMS or O_2. These results confirmed the ROS were generated from both PMS and O_2. In addition, due to the VB of Fe_1/TiO_2-O_V (1.96 eV) being negative than $H_2O/\bullet OH$ (2.40 eV), it was difficult for $\bullet OH$ generation from water combining with h^+, while, $\bullet OH$ could be generated by water combining with the $\bullet SO_4^-$ that arising from PMS, which was further proved by no $\bullet OH$ signal obtained from the EPR identification in absent of PMS (Fig. S18a).

Determining the role of each reactive species is essential since the phenol oxidation process may involve many reactive species, such as photogenerated electrons (e^-), holes (h^+), $\bullet OH$, $\bullet SO_4^-$, $\bullet O_2^-$ and $^1O_2$. To this end, we selected $AgNO_3$, ethylene glycol (EG), methyl alcohol (MeOH), ascorbic acid (AA), and 2,2,6,6-tetramethylpiperidine (TEMP) as the scavengers for e^-, h^+, $\bullet OH$, $\bullet SO_4^-$, $\bullet O_2^-$ and $^1O_2$, respectively. As shown in Fig. S19, all scavengers were found to effectively inhibit the activity of phenol oxidative degradation, which highlighted the importance of cooperation in all reactive species for phenol activation and conversion.
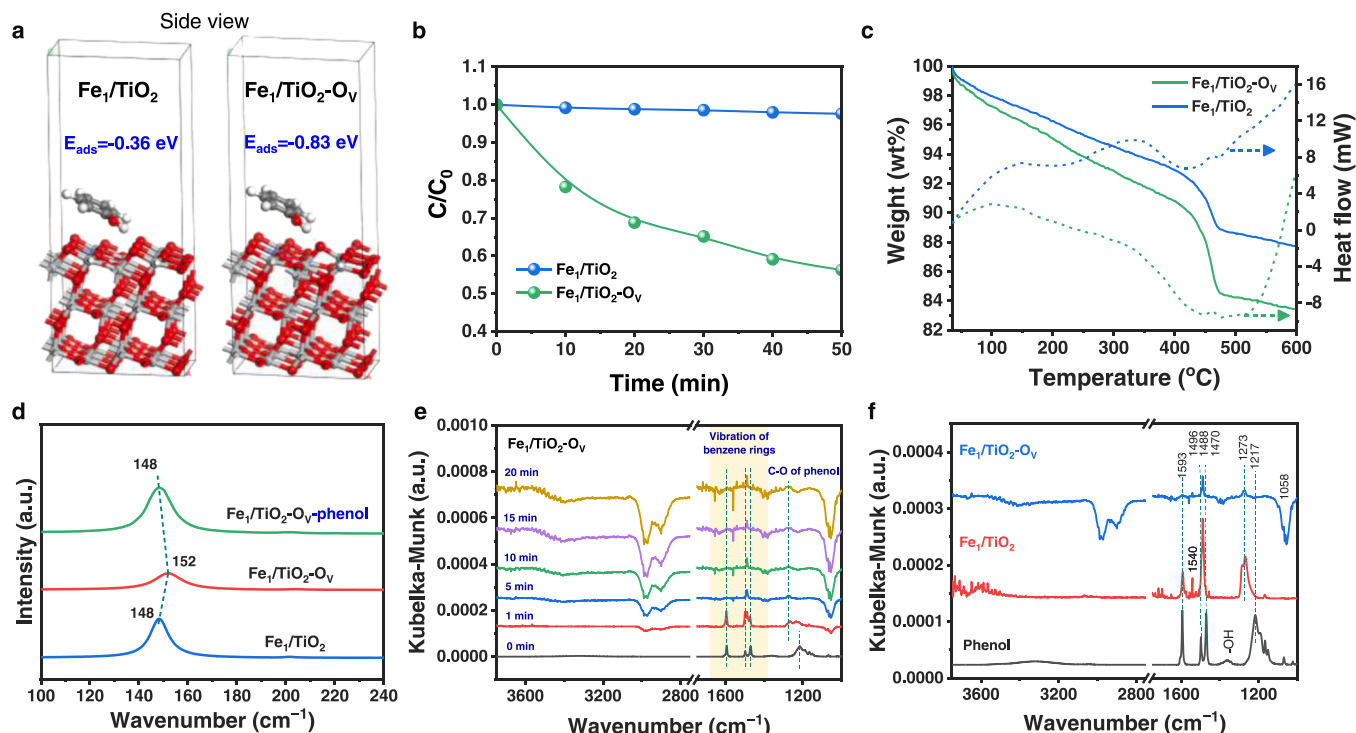
Fig. 7. (a) Calculated adsorption energy of phenol on Fe$_1$/TiO$_2$ (left) and Fe$_1$/TiO$_2$-O$_V$ (right); (b) The adsorption effectivity (c) and TGA-DSC curves for Fe$_1$/TiO$_2$ and Fe$_1$/TiO$_2$-O$_V$ catalyst; (d) In-situ Raman on Fe$_1$/TiO$_2$-O$_V$ with phenol adsorption; (e) In-situ ATR-IR of phenol adsorption on Fe$_1$/TiO$_2$-O$_V$ within 20 min at 30 °C under visible light; (f) In-situ ATR-IR of phenol adsorption on Fe$_1$/TiO$_2$ and Fe$_1$/TiO$_2$-O$_V$ at 5 min at 30 °C under visible light.

3.5. Phenol adsorption and activation

It is well known that the reactant molecular adsorption on the catalyst surface is the first and important step in the heterogeneous catalytic process. Thus, the influence of oxygen vacancies on the adsorption of phenol was further investigated. Firstly, we calculated the phenol adsorption energy (E$_{ads}$) on the surface of Fe$_1$/TiO$_2$-O$_V$, Fe$_1$/TiO$_2$, TiO$_2$-O$_V$ and TiO$_2$ by the DFT method. The model for Fe$_1$/TiO$_2$-O$_V$ and Fe$_1$/TiO$_2$ are displayed in Fig. S20, respectively. As shown in Fig. S21, when phenol was adsorbed on the surface of catalysts, it preferred to stabilize on the O$_V$ rather than Fe single atoms. Given that the E$_{ads}$ value of Fe$_1$/TiO$_2$-O$_V$ (−0.83 eV) was obviously lower than that of Fe$_1$/TiO$_2$ (−0.36 eV), revealing the existence of O$_V$ was more conducive to the adsorption of phenol (Fig. 7a, Fig. S22 and Table S10), which might result from the O$_V$ acting as sites to adsorb phenol via hydroxyl group (-OH) to O$_V$ [13,14]. Similarly, the E$_{ads}$ value of TiO$_2$-O$_V$ (−0.35 eV) was obviously lower than that of TiO$_2$ (−0.04 eV), further confirming the adsorption of phenol on O$_V$ (Fig. S23 and Table S10). Moreover, the decrease for the E$_{ads}$ value of Fe$_1$/TiO$_2$-O$_V$ compared to that of TiO$_2$-O$_V$ might be attributed to the regulation for electronic state of oxygen atoms around O$_V$ by adjacent Fe single atom, so as to boost the adsorption of phenol. Therefore, it could be preliminarily concluded that Fe$_1$/TiO$_2$-O$_V$ with abundant oxygen vacancies had the robust ability for phenol adsorption.

An insight into phenol adsorption was next measured by a control experiment and TGA-DSC. The phenol adsorption kinetic can be observed in Fig. 7b. It can be seen that Fe$_1$/TiO$_2$-O$_V$ had higher adsorption capacity for phenol with respect to Fe$_1$/TiO$_2$ catalyst. In the meanwhile, desorption process was determined by TGA-DSC. In Fig. 7c, the weight loss of 16.6% and 12.3% from phenol deposition was observed in Fe$_1$/TiO$_2$-O$_V$ and Fe$_1$/TiO$_2$ catalysts, respectively. Thus, Fe$_1$/TiO$_2$-O$_V$ catalyst exhibited a higher desorption amount for phenol compared with Fe$_1$/TiO$_2$, hinting that phenol can be efficiently adsorbed and activated on the surface of Fe$_1$/TiO$_2$-O$_V$, which might be resulted from its higher O$_V$ concentration [64], agreeing well with DFT calculations.

To further investigate where the phenol adsorbed, the in-situ Raman was performed to monitor the oxygen vacancies fluctuation after the adsorption of phenol. As shown in Fig. 7d, oxygen vacancies induced the ν(O-Ti-O) modes of Fe$_1$/TiO$_2$-O$_V$ catalyst blueshifted from 148 to 152 cm^{-1} with respect to Fe$_1$/TiO$_2$. As expected, after phenol was injected phenol into the sample, the redshift of ν(O-Ti-O) modes occurred and it restored to 148 cm^{-1}. Identically, the ν(O-Ti-O) modes of TiO$_2$-O$_V$ catalyst redshifted from 152 to 148 cm^{-1} after phenol was introduced (Fig. S24). This result strongly verified the adsorption of phenol was on the surface oxygen vacancies.

Furthermore, we used in-situ ATR-IR to monitor the phenol adsorption and next activation on Fe$_1$/TiO$_2$-O$_V$ and Fe$_1$/TiO$_2$. As shown in Fig. 7e, after dropping phenol on the Fe$_1$/TiO$_2$-O$_V$ catalyst, the intensity of the C-O-H bond (1217 cm^{-1}) gradually decreased and finally disappeared. Corresponding, a peak at 1273 cm^{-1} appeared, which can be ascribed to the absorption of -OH on the unsaturated coordinated Ti or the transformation of -OH by ROS (•OH) thereafter dehydration [65–67]. Combining with the results of DFT calculations and Raman spectra, it can be concluded that the hydroxyl group adsorbed on the oxygen vacancies of Fe$_1$/TiO$_2$-O$_V$ catalyst for the next activation of the benzene ring in phenol, while the hydroxyl group was directly oxidized on the surface of Fe$_1$/TiO$_2$ catalyst due to the lack of adsorbed sites. This was further confirmed by the transformation of 1593 cm^{-1}, 1496 cm^{-1} and 1470 cm^{-1} peaks, attributed to ν(C-C) in the benzene ring of phenol [68], in the phenol/catalyst system. From Fig. 7f, one can see that after 5 min for phenol adsorption on the surface of Fe$_1$/TiO$_2$-O$_V$ catalyst under visible light, 1593 cm^{-1} and 1496 cm^{-1} peaks disappeared and the intensity of 1470 cm^{-1} peak decreased significantly as well as shifted to higher wavenumber (1488 cm^{-1}), which suggested that the benzene ring was opened effectively. On the contrary, the intensity of 1593 cm^{-1}, 1496 cm^{-1} and 1488 cm^{-1} peaks in the phenol/Fe$_1$/TiO$_2$ catalyst system decreased slightly, indicating that the ROS preferred to attack hydroxyl groups rather than the benzene ring of phenol in phenol/Fe$_1$/TiO$_2$ system. Moreover, the obvious 1540 cm^{-1} peak attributed
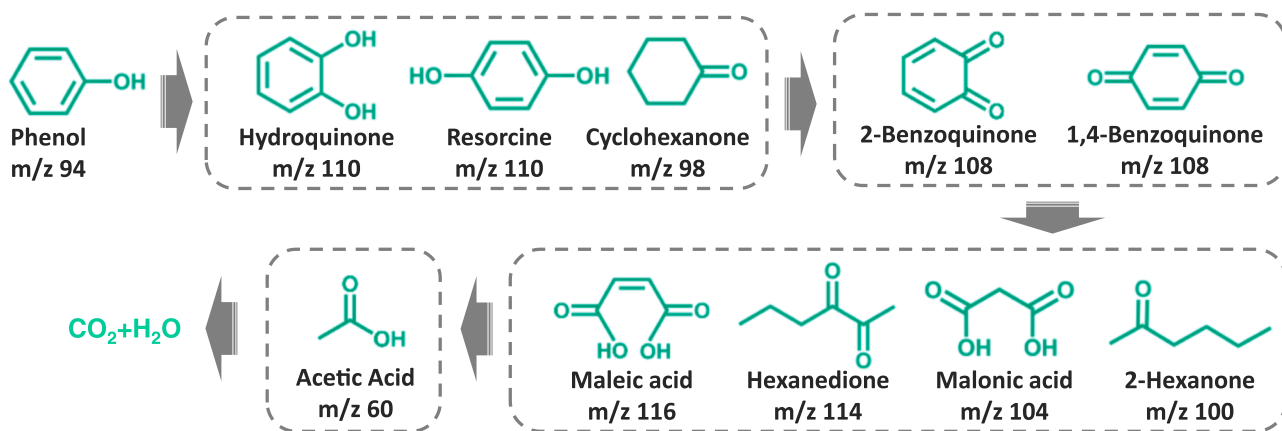
Fig. 8. Intermediates identification of phenol photo-Fenton catalytic oxidation by GC-MS.
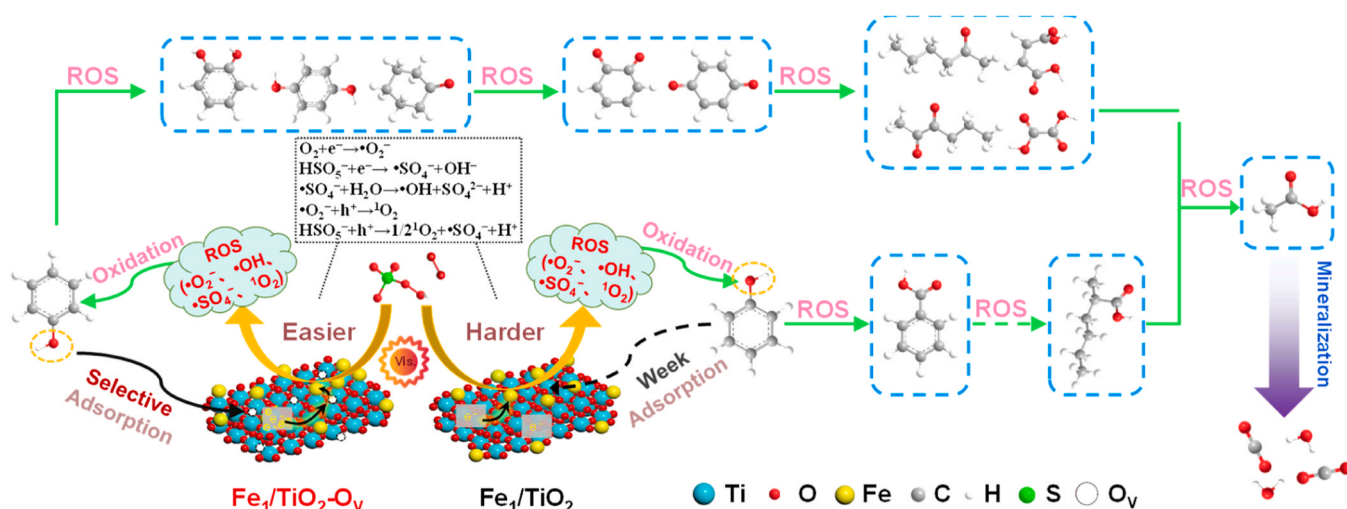

Fig. 9. The proposed mechanism for photo-Fenton catalytic oxidation of phenol on Fe_1/TiO_2-O_V catalyst.

to carboxide in the phenol/Fe_1/TiO_2 catalyst system [67] and the 1058 cm^{-1} peak attributed to cyclohexanol in the phenol/Fe_1/TiO_2-O_V catalyst system [67] further confirmed that the oxygen vacancies are conductive to adsorb hydroxyl groups of phenol, which facilitate the opening of benzene ring in phenol.

At last, a GC-MS test was performed to elucidate the evolution process of phenol conversion on Fe_1/TiO_2-O_V catalyst. In Fig. 8, Fig. S25 and Table S11, it could be clearly seen that the phenol oxidation process could be as follows: (i) the hydrogen atoms on the benzene ring of phenol were extracted to form hydroxyls. Then, hydroxyls were gradually oxidized to aldehydes and carboxyls. Finally, the benzene ring was mineralized. (Primary pathway) (ii) Also, another route was displayed that the benzene ring was hydrogenated firstly by photogenerated electrons and formed cyclohexanone. Thereafter, the 2-hexanone intermediate was generated and finally transformed to CO_2 and H_2O.

Combining with the results of DFT, TGA-DSC, in-situ Raman, in-situ ATR-IR and GC-MS, the possible mechanisms of photo-Fenton catalytic phenol oxidation over Fe_1/TiO_2-O_V can be proposed and depicted in Fig. 9. Firstly, the phenol adsorbs on the surface of Fe_1/TiO_2-O_V catalyst via hydroxyl group (-OH) to O_V. Secondly, under the visible-light irradiation, the Fe single atoms and oxygen vacancies synergistically promote the photogenerated electrons and holes separation, and then the photogenerated electrons directionally transfer and accumulate on Fe single sites via O_V, which is conducive to the reduction of O_2 to $\bullet O_2^-$ and the activation of PMS to $\bullet OH/\bullet SO_4^-$. For photogenerated holes, they can oxidate the $\bullet O_2^-$ and PMS to $^1O_2$ [69,70]. Then, the phenol adsorbed on

the oxygen vacancies can be attacked fast by sufficient oxygen active species ($\bullet O_2^-$, $\bullet OH$, $\bullet SO_4^-$ and $^1O_2$) or photogenerated electrons/holes for ring-opening intermediate generation. Finally, phenol is mineralized into CO_2 and H_2O. In this process, according to the references, we believe the generation of $^1O_2$ contributes to the hydroxylation of phenol which can enhance the polarity of phenol molecule, consequently promote its adsorption on the catalyst surface and finally improve the degradation activity [71]. In this case the $\bullet OH$ dominates the initial activation of phenol molecule, which can directly convert phenol into dehydroxylated compounds [72,73]. These compound intermediates are further oxidized by $\bullet OH$, $\bullet O_2^-$ and $\bullet SO_4^-$ to break the benzene ring to produce small organic acids, and finally to CO_2 and H_2O [74–76].

4. Conclusion

In summary, we have proposed a defect strategy in single-atom catalyst for remarkably boosted photo-Fenton process. Firstly, microstructural characterizations indicated abundant oxygen vacancies have been successfully introduced to Fe_1/TiO_2 single-atom catalyst. Unlike little catalysis observed on Fe_1/TiO_2, TiO_2-O_V and TiO_2 samples, Fe_1/ TiO_2-O_V catalyst resulted in an order of magnitude increase in phenol oxidation rate (0.0814 min^{-1}), which revealed the significant synergy between atomically dispersed Fe species and oxygen vacancies. Structural analysis, XPS, Raman, IR spectroscopic measurements, EPR measurements and DFT calculations demonstrated that (1) oxygen vacancies worked as electron trap under light illumination, promoting the electron

density of Fe single sites through the oriented delivery of photo-generated electrons, which led to highly efficient generation of ROS; (2) advantageous adsorption of phenol on oxygen vacancies was conductive to the subsequent oxidation. In particular, due to the selective adsorption of hydroxyl on oxygen vacancies, the benzene ring of phenol was selectively attacked and then opened by abundant ROS. As a result, Fe_1/TiO_2-O_V catalyst exhibited the superior mineralization ability for phenol and the mineralization pathways were also presented through GC-MS. This work provides insights into heterogeneous single-atom photocatalysts and oxygen vacancies, which plays an important role in photo-Fenton catalytic phenol oxidation and could be generally applied as design principles for photo-Fenton catalytic phenol oxidation with improved activity.

CRediT authorship contribution statement

Man Yang: Writing – review & editing, Writing – original draft, Supervision, Methodology, Funding acquisition, Conceptualization. **Haibo Li:** Methodology, Investigation, Formal analysis. **Fenli Liu:** Methodology, Investigation, Formal analysis. **Shaodong Sun:** Writing – review & editing, Supervision, Funding acquisition. **Jie Cui:** Formal analysis. **Yang Xu:** Formal analysis. **Jing Mei:** Formal analysis. **Yuxiang Jiao:** Formal analysis. **Hailiang Song:** Investigation. **Zongfan Duan:** Investigation. **Wengang Liu:** Supervision, Methodology, Investigation. **Yujing Ren:** Writing – review & editing, Supervision, Project administration, Funding acquisition.

Declaration of Competing Interest

The authors declare that they have no known competing financial interests or personal relationships that could have appeared to influence the work reported in this paper.

Data Availability

Data will be made available on request.

Acknowledgements

Appendix A. Supporting information

Supplementary data associated with this article can be found in the online version at doi:10.1016/j.apcatb.2024.124071.

References

[1] F.W. Owa, Water pollution: sources, effects, control and management, Mediterr. J. Soc. Sci. 4 (2013) 65.

[2] B. Sarker, K.N. Keya, F. Mahir, K. Nahiun, S. Shahida, R. Khan, Surface and ground water pollution: causes and effects of urbanization and industrialization in South Asia, Sci. Rev. 7 (2021) 32–41.

[3] S. Ahmed, M.G. Rasul, W.N. Martens, R. Brown, M.A. Hashib, Heterogeneous photocatalytic degradation of phenols in wastewater: a review on current status and developments, Desalination 261 (2010) 3–18.

[4] H.F. Stich, The beneficial and hazardous effects of simple phenolic compounds, Mutat. Res. Genet. Toxen. 259 (1991) 307–324.

[5] J.J. Delfino, D.J. Dube, Persistent contamination of ground water by phenol, J. Environ. Sci. Heal. A 11 (1976) 345–355.

[6] R.K. Vedula, S. Dalal, C.B. Majumder, Bioremoval of cyanide and phenol from industrial wastewater: an update, Bioremediat. J. 17 (2013) 278–293.

[7] R. Wang, L. Du, W. Gao, J. Li, N.T. Tsona, X. Zhang, X. Hu, W. Wang, H. Liu, Enhanced photocatalytic performance of PdO-loaded heterostructured nanobelts to degrade phenol, Chemosphere 276 (2021) 130266.

[8] Z. Wang, Y. Wang, Y. Zhang, X. Sun, Y. Lou, Y. Zhang, Y. Dong, C. Pan, Y. Zhu, Efficient photothermal degradation on $Bi_{12}CoO_{20}$ sillenite with a strong internal electric field induced by the thermal effect, Appl. Catal. B: Environ. 313 (2022) 121452.

[9] H. Huang, R. Shi, X. Zhang, J. Zhao, C. Su, T. Zhang, Photothermal-assisted triphase photocatalysis over a multifunctional bilayer paper, Angew. Chem. 133 (2021) 23145–23151.

[10] J. Li, X. Yang, C. Ma, Y. Lei, Z. Cheng, Z. Rui, Selectively recombining the photoinduced charges in bandgap-broken $Ag_3PO_4/GdCrO_3$ with a plasmonic Ag bridge for efficient photothermocatalytic VOCs degradation and CO_2 reduction, Appl. Catal. B: Environ. 291 (2021) 120053.

[11] L. Chen, W. Cui, J. Li, H. Wang, X.A. Dong, P. Chen, Y. Zhou, F. Dong, The high selectivity for benzoic acid formation on $Ca_2Sb_2O_7$ enables efficient and stable toluene mineralization, Appl. Catal. B: Environ. 271 (2020) 118948–118957.

[12] S. Zhou, Y. Wang, K. Zhou, D. Ba, Y. Ao, P. Wang, In-situ construction of Z-scheme g-C_3N_4/WO_3 composite with enhanced visible-light responsive performance for nitenpyram degradation, Chin. Chem. Lett. 32 (2021) 2179–2182.

[13] M. Yang, K. Wu, S. Sun, Y. Ren, Regulating oxygen defects via atomically dispersed alumina on Pt/WO_x catalyst for enhanced hydrogenolysis of glycerol to 1,3-propanediol, Appl. Catal. B: Environ. 307 (2022) 121207.

[14] Y. Niu, B. Zhao, Y. Liang, L. Liu, J. Dong, Promoting role of oxygen deficiency on a WO_3-Supported Pt catalyst for glycerol hydrogenolysis to 1,3-propanediol, Ind. Eng. Chem. Res. 59 (2020) 7389–7397.

[15] M. Yang, K. Wu, S. Sun, J. Duan, X. Liu, J. Cui, S. Liang, Y. Ren, Unprecedented relay catalysis of curved Fe_1–N_4 single-atom site for remarkably efficient $^1O_2$ generation, ACS Catal. 13 (2023) 681–691.

[16] L. Xiong, H. Qi, S. Zhang, L. Zhang, X. Liu, A. Wang, J. Tang, Highly selective transformation of biomass derivatives to valuable chemicals by single-atom photocatalyst Ni/TiO_2, Adv. Mater. 35 (2023) 2209646.

[17] M. Yang, J. Mei, Y. Ren, J. Cui, S. Liang, S. Sun, Long-range electron synergy over Pt_1-Co_1/CN bimetallic single-atom catalyst in enhancing charge separation for photocatalytic hydrogen production, J. Energy Chem. 81 (2023) 502–509.

[18] L. Su, P. Wang, X. Ma, J. Wang, S. Zhan, Regulating local electron density of iron single sites by introducing nitrogen vacancies for efficient photo-Fenton process, Angew. Chem. Int. Ed. 60 (2021) 21261–21266.

[19] M. Qian, X.-L. Wu, M. Lu, L. Huang, W. Li, H. Lin, J. Chen, S. Wang, X. Duan, Modulation of charge trapping by island-like single-atom cobalt catalyst for enhanced photo-Fenton-like reaction, Adv. Funct. Mater. 33 (2023) 2208688.

[20] X. Mi, P. Wang, S. Xu, L. Su, H. Zhong, H. Wang, Y. Li, S. Zhan, Almost 100% peroxymonosulfate conversion to singlet oxygen on single-atom CoN_{2+2} sites, Angew. Chem. Intern. Ed. 60 (2021) 4588–4593.

[21] J. Duan, Y. Zhou, Y. Ren, F. Liu, P. Deng, M. Yang, H. Ge, J. Gao, J. Yang, Y. Qin, Effect of electronic structure over late transition-metal M_1–N_4 single-atom sites on hydroxyl radical-induced oxidations, ACS Catal. 13 (2023) 3308–3316.

[22] R. Yanagi, T. Zhao, D. Solanki, Z. Pan, S. Hu, Charge separation in photocatalysts: mechanisms, physical parameters, and design principles, ACS Energy Lett. 7 (2022) 432–452.

[23] S. Ji, Y. Chen, X. Wang, Z. Zhang, D. Wang, Y. Li, Chemical synthesis of single atomic site catalysts, Chem. Rev. 120 (2020) 11900–11955.

[24] J. Li, Q. Guan, H. Wu, W. Liu, Y. Lin, Z. Sun, X. Ye, X. Zheng, X. Pan, J. Zhu, S. Chen, W. Zhang, S. Wei, J. Lu, Highly active and stable metal single-atom catalysts achieved by strong electronic metal–support interactions, J. Am. Chem. Soc. 141 (2019) 14515–14519.

[25] T. Wang, T. Zhu, Z. Luo, Y. Li, J. Niu, C. Wang, Oxygen vacancy confining effect on photocatalytic efficiency of Pt_1-black TiO_2 single-atom photocatalysts for hydrogen generation and phenol decomposition, Environ. Chem. Lett. 19 (2021) 1815–1821.

[26] J. Cai, A. Cao, Z. Wang, S. Lu, Z. Jiang, X. Dong, X. Li, S. Zang, Surface oxygen vacancies promoted Pt redispersion to single-atoms for enhanced photocatalytic hydrogen evolution, J. Mater. Chem. A 9 (2021) 13890–13897.

[27] T.C. Khiem, N.N. Huy, E. Kwon, J. Lee, W.D. Oh, X.G. Duan, S. Waclawek, H. T. Wang, G. Lisak, F. Ghanbari, K.Y.A. Lin, Electron transfer-mediated enhancement of superoxide radical generation in Fenton-like process: Key role of oxygen vacancy-regulated local electron density of cobalt sites, Appl. Catal. B: Environ. 343 (2023) 123490.

[28] G. Wang, T. Huo, Q. Deng, F. Yu, Y. Xia, H. Li, W. Hou, Surface-layer bromine doping enhanced generation of surface oxygen vacancies in bismuth molybdate for efficient photocatalytic nitrogen fixation, Appl. Catal. B: Environ. 310 (2022) 121319.

[29] M. Yang, L. He, Z. Shi, J. Mei, C. Liu, B. Yang, J. Cui, S. Liang, S. Sun, An unprecedented strategy to fabricate inside/surface homojunction in bismuth oxychloride for efficient photocatalysis, J. Phys. Chem. C. 127 (2023) 4570–4581.

[30] Z. Hu, X. Li, S. Zhang, Q. Li, J. Fan, X. Qu, K. Lv, Fe_1/TiO_2 Hollow microspheres: Fe and Ti dual active sites boosting the photocatalytic oxidation of NO, Small 16 (2022) 2004583.

[31] X. Zhang, C. Li, X. Wang, S. Yang, Y. Tan, F. Yuan, F. Zheng, D.D. Dionysiou, Z. Sun, Defect engineering modulated iron single atoms with assist of layered clay for enhanced advanced oxidation processes, Small 18 (2022) 2204793.

[32] F. Mo, C. Song, Q. Zhou, W. Xue, S. Ouyang, Q. Wang, Z. Hou, S. Wang, J. Wang, The optimized Fenton-like activity of Fe single-atom sites by Fe atomic clusters–mediated electronic configuration modulation, PNAS 120 (2023) e2300281120.

[33] T.C. Khiem, N.N. Huy, E. Kwon, J. Lee, W.D. Oh, X. Duan, S. Wacławek, H. Wang, G. Lisak, F. Ghanbari, K.A. Lin, Electron transfer-mediated enhancement of superoxide radical generation in fenton-like process: Key role of oxygen vacancy-regulated local electron density of cobalt sites, Appl. Catal. B: Environ. 343 (2024) 123490.

[34] P. Deng, J. Duan, F. Liu, N. Yang, H. Ge, J. Gao, H. Qi, D. Feng, M. Yang, Y. Qin, Y. Ren, Atomic insights into synergistic nitroarene hydrogenation over nanodiamond-supported Pt_1-Fe_1 dual-single-atom catalyst, Angew. Chem. Int. Ed. 62 (2023) e202307853.

[35] B. Singh, M.B. Gawande, A.D. Kute, R.S. Varma, P. Fornasiero, P. McNeice, R. V. Jagadeesh, M. Beller, R. Zbořil, Single-atom (iron-based) catalysts: synthesis and applications, Chem. Rev. 121 (2021) 13620–13697.

[36] Y. Liu, X. Liu, Z. Lv, R. Liu, L. Li, J. Wang, W. Yang, X. Jiang, X. Feng, B. Wang, Tuning the spin state of the iron center by bridge-bonded Fe-O-Ti ligands for enhanced oxygen reduction, Angew. Chem. Int. Ed. 61 (2022) e202117617.

[37] R. Jia, Y. Wang, C. Wang, Y. Ling, Y. Yu, B. Zhang, Boosting selective nitrate electroreduction to ammonium by constructing oxygen vacancies in TiO_2, ACS Catal. 10 (2020) 3533–3540.

[38] D. Montalvo, G. Corro, F. Bañuelos, O. Olivares-Xometl, P. Arellanes, U. Pal, Selective alcohols production through CO_2 photoreduction using Co_3O_4/TiO_2 photocatalyst exploiting synergetic interactions between Ti^{3+}, Co^{2+} and Co^{3+}, Appl. Catal. B: Environ. 330 (2023) 122652.

[39] Y. Wang, Y. Zhang, X. zhu, Y. Liu, Z. Wu, Fluorine-induced oxygen vacancies on TiO_2 nanosheets for photocatalytic indoor VOCs degradation, Appl. Catal. B: Environ. 316 (2022) 121610.

[40] S. Wang, L. Pan, J.-J. Song, W. Mi, J.-J. Zou, L. Wang, X. Zhang, Titanium-defected undoped anatase TiO_2 with p-Type conductivity, room-temperature ferromagnetism, and remarkable photocatalytic performance, J. Am. Chem. Soc. 137 (2015) 2975–2983.

[41] L. Wang, E. Guan, J. Zhang, J. Yang, Y. Zhu, Y. Han, M. Yang, C. Cen, G. Fu, B. C. Gates, F.-S. Xiao, Single-site catalyst promoters accelerate metal-catalyzed nitroarene hydrogenation, Nat. Commun. 9 (2018) 1362.

[42] M. Thommes, K. Kaneko, A.V. Neimark, J.P. Olivier, F. Rodriguez-Reinoso, J. Rouquerol, K.S.W. Sing, Physisorption of gases, with special reference to the evaluation of surface area and pore size distribution (IUPAC Technical Report), Pure Appl. Chem. 87 (2015) 1051–1069.

[43] X. Jia, J. Zhang, Q. Huang, C. Xiong, H. Ji, Q. Ren, F. Huang, S. Chen, Z. Jin, J. Chen, W. Guo, Y. Ge, Y. Ding, Heterogeneous catalytic degradation of phenol by $CuFe_2O_4/Bi_{12}O_{15}Cl_6$ photocatalyst activated peroxymonosulfate, Mater. Res. Bull. 167 (2023) 112435.

[44] S. Wang, W. An, Z. Lu, L. Liu, J. Hu, Y. Liang, W. Cui, A $Cu/CuFe_2O_4$-OVs two-electron centre-based synergistic photocatalysis-Fenton system for efficient degradation of organic pollutants, Chem. Eng. J. 441 (2022) 135944.

[45] W. An, H. Wang, T. Yang, J. Xu, Y. Wang, D. Liu, J. Hu, W. Cui, Y. Liang, Enriched photocatalysis-Fenton synergistic degradation of organic pollutants and coking wastewater via surface oxygen vacancies over Fe-BiOBr composites, Chem. Eng. J. 451 (2023) 138653.

[46] A.A.P. Khan, P. Raizada, P. Singh, A. Khan, M.O. Ansari, M.M. Alotaibi, A. Z-scheme, photocatalysis for phenol eradication from water using peroxymonosulfate activation Ag/AgBr/SCN nanocomposite, J. Taiwan Inst. Chem. E. 144 (2023) 104722.

[47] Q. Wang, N. Li, M. Tan, M. Deng, G. Yang, Q. Li, H. Du, Novel dual Z-scheme Bi/BiOI-Bi₂O₃-C₃N₄ heterojunctions with synergistic boosted photocatalytic degradation of phenol, Sep. Purif. Technol. 307 (2023) 122733.

[48] M. Arumugam, R. Koutavarapu, K.K. Seralathan, P. Praserthdam, P. Praserthdam, Noble metals (Pd, Ag, Pt, and Au) doped bismuth oxybromide photocatalysts for improved visible light-driven catalytic activity for the degradation of phenol, Chemosphere 324 (2023) 138368.

[49] A. Sarwar, A. Razzaq, M. Zafar, I. Idrees, F. Rehman, W.Y. Kim, Copper tungstate ($CuWO_4$)/graphene quantum dots (GQDs) composite photocatalyst for enhanced degradation of phenol under visible light irradiation, Results Phys. 45 (2023) 106253.

[50] H. Zhang, C. Wang, L. Li, J. Zhang, J. Zhao, T. Sun, B. Cui, 3D-crumpled graphitic carbon nitride achieving promoted visible-light-driven molecular oxygen activation for phenol degradation, Chemosphere 321 (2023) 138107.

[51] C. Xu, Z. Jin, J. Yang, F. Guo, P. Wang, H. Meng, G. Bao, Z. Li, C. Chen, F. Liu, R. Hu, A direct Z-scheme $LaFeO_3/WO_3$ photocatalyst for enhanced degradation of phenol under visible light irradiation, J. Environ. Chem. Eng. 9 (2021) 106337.

[52] J. Wei, X. Feng, X. Hu, J. Yang, C. Yang, B. Liu, Cu(II) doped FeOCl as an efficient photo-Fenton catalyst for phenol degradation at mild pH, Colloid Surf. A. 631 (2021) 127754.

[53] C. Xu, Z. Jin, J. Yang, J. Cui, J. Hu, Z. Li, C. Chen, F. Liu, R. Hu, High surface area B-doped $LaFeO_3/Ag/Ag_3PO_4$ as a Z-scheme photocatalyst for facilitate phenol degradation, Colloid Surf. A. 651 (2022) 129668.

[54] R. Ji, J. Liu, T. Zhang, Y. Peng, Y. Li, D. Chen, Q. Xu, J. Lu, Construction of a ternary Z-scheme $In_2S_3@Au/P3HT$ photocatalyst for the degradation of phenolic pollutants under visible light, Sep. Purif. Technol. 272 (2021) 118787.

[55] I. Ali, J.-O. Kim, Optimization of photocatalytic performance of a $gC_3N_4–TiO_2$ nanocomposite for phenol degradation in visible light, Mater. Chem. Phys. 261 (2021) 124246.

[56] Y. Yuan, R.-T. Guo, L.-F. Hong, Z.-D. Lin, X.-Y. Ji, W.-G. Pan, Fabrication of a dual S-scheme $Bi_7O_9I_3/g-C_3N_4/Bi_3O_4Cl$ heterojunction with enhanced visible-light-driven performance for phenol degradation, Chemosphere 287 (2022) 132241.

[57] M. Moradi, Y. Vasseghian, A. Khataee, M. Harati, H. Arfaeinia, Ultrasound-assisted synthesis of $FeTiO_3/GO$ nanocomposite for photocatalytic degradation of phenol under visible light irradiation, Sep. Purif. Technol. 261 (2021) 118274.

[58] W. Zhang, H. He, H. Li, L. Duan, L. Zu, Y. Zhai, W. Li, L. Wang, W. Fu, D. Zhao, Visible-light responsive TiO_2-based materials for efficient solar energy utilization, Adv. Energy Mater. 11 (2021) 2003303.

[59] X. Li, B. Kang, F. Dong, Z. Zhang, X. Luo, L. Han, J. Huang, Z. Feng, Z. Chen, J. Xu, B. Peng, Z.L. Wang, Enhanced photocatalytic degradation and H_2/H_2O_2 production performance of $S-pCN/WO_{2.72}$ S-scheme heterojunction with appropriate surface oxygen vacancies, Nano Energy 81 (2021) 105671.

[60] Y. Wang, X. Li, S. Liu, Y. Liu, T. Kong, H. Zhang, X. Duan, C. Chen, S. Wang, Roles of catalyst structure and gas surface reaction in the generation of hydroxyl radicals for photocatalytic oxidation, ACS Catal. 12 (2022) 2770–2780.

[61] J. Schneider, M. Matsuoka, M. Takeuchi, J. Zhang, Y. Horiuchi, M. Anpo, D. W. Bahnemann, Understanding TiO_2 photocatalysis: Mechanisms and materials, Chem. Rev. 114 (2014) 9919–9986.

[62] R. Qian, H. Zong, J. Schneider, G. Zhou, T. Zhao, Y. Li, J. Yang, D.W. Bahnemann, J.H. Pan, Charge carrier trapping, recombination and transfer during TiO_2 photocatalysis: An overview, Catal. Today 335 (2019) 78–90.

[63] C. Kranz, M. Wächtler, Characterizing photocatalysts for water splitting: from atoms to bulk and from slow to ultrafast processes, Chem. Soc. Rev. 50 (2021) 1407–1437.

[64] X. Wei, K. Li, X. Zhang, Q. Tong, J. Ji, Y. Cai, B. Gao, W. Zou, L. Dong, CeO_2 nanosheets with anion-induced oxygen vacancies for promoting photocatalytic toluene mineralization: Toluene adsorption and reactive oxygen species, Appl. Catal. B: Environ. 317 (2022) 121694.

[65] A. Zuber, G. Tsilomelekis, Acidity-activity relationships in the solvent-free tert-butylation of phenol over sulfated metal oxides, Appl. Catal. A: Gen. 652 (2023) 119040.

[66] O. D'Alessandro, H. Thomas, J.E. Sambeth, Removal of phenol from aqueous solutions by adsorption onto Mn–Ce–K solids, React. Kinet. Mech. Catal. 113 (2014) 257–267.

[67] P.M. de Souza, R.C. Rabelo-Neto, L.E.P. Borges, G. Jacobs, B.H. Davis, D. E. Resasco, F.B. Noronha, Hydrodeoxygenation of phenol over Pd Catalysts. Effect of support on reaction mechanism and catalyst deactivation, ACS Catal. 7 (2017) 2058–2073.

[68] S. Horikoshi, T. Miura, M. Kajitani, H. Hidaka, N. Serpone, A. FT-IR, DRIFT) study of the influence of halogen substituents on the TiO_2-assisted photooxidation of phenol and p-halophenols under weak room light irradiance, J. Photoch. Photobio. A 194 (2008) 189–199.

[69] Y. Nosaka, A.Y. Nosaka, Generation and detection of reactive oxygen species in photocatalysis, Chem. Rev. 117 (2017) 11302–11336.

[70] Z. Weng, Y. Lin, B. Han, X. Zhang, Q. Guo, Y. Luo, X. Ou, Y. Zhou, J. Jiang, Donor-acceptor engineered $g-C_3N_4$ enabling peroxymonosulfate photocatalytic conversion to $^1O_2$ with nearly 100% selectivity, J. Hazard. Mater. 448 (2023) 130869.

[71] H. Yu, D. Liu, H. Wang, H. Yu, Q. Yan, J. Ji, J. Zhang, M. Xing, Singlet oxygen synergistic surface-adsorbed hydroxyl radicals for phenol degradation in CoP catalytic photo-Fenton, Chin. J. Catal. 43 (2022) 2678–2689.3.

[72] N. Agarwal, S.J. Freakley, R.U. McVicker, S.M. Althahban, N. Dimitratos, Q. He, D. J. Morgan, R.L. Jemkins, D.J. Willock, S.H. Taylor, C.J. Kiely, G.J. Hutchings, Aqueous Au-Pd colloids catalyze selective CH_4 oxidation to CH_3OH with O_2 under mild conditions, Science 358 (2017) 223–227.

[73] Q. Zhou, X. Tan, X. Wang, Q. Zhang, C. Qi, H. Yang, Z. He, T. Xing, M. Wang, M. Wu, W. Wu, Selective photocatalytic oxidation of methane to methanol by constructing a rapid O_2 conversion pathway over Au–Pd/ZnO, ACS Catal. 14 (2024) 955–964.

[74] L. Yang, Z. Chen, Q. Cao, H. Liao, J. Gao, L. Zhang, W. Wei, H. Li, J. Lu, Structural regulation of photocatalyst to optimize hydroxyl radical production pathways for highly efficient photocatalytic oxidation, Adv. Mater. 36 (2024) 2306758.

[75] D. Ma, J. Zhong, J. Li, C. Burda, R. Duan, Preparation and photocatalytic performance of MWCNTs/BiOCl: Evidence for the superoxide radical participation in the degradation mechanism of phenol, Appl. Surf. Sci. 480 (2019) 395–403.

[76] X. Li, X. Min, X. Hu, Z. Jiang, C. Li, W. Yang, F. Zhao, In-situ synthesis of highly dispersed Cu-Cu_xO nanoparticles on porous carbon for the enhanced persulfate activation for phenol degradation, Sep. Purif. Technol. 276 (2021) 119260.